Electrospun generation of Ti$_3$C$_2$T$_x$ MXene@graphene oxide hybrid aerogel microspheres for tunable high-performance microwave absorption

Ying Li, Fanbin Meng*, Yuan Mei, Huagao Wang, Yifan Guo, Ying Wang, Fuxi Peng, Fei Huang, Zuowan Zhou*

Key Laboratory of Advanced Technologies of Materials (Ministry of Education), School of Materials Science and Engineering, Southwest Jiaotong University, Chengdu 610031, China

HIGHLIGHTS

- Synthesized a new kind of Ti$_3$C$_2$T$_x$ MXene@GO hybrid aerogel microspheres.
- RL$_{min}$ value of -49.1 dB at 1.2 mm with loading of 10 wt% was achieved.
- The hybrid aerogel exhibited excellent attenuating ability in S band.
- Multiple attenuation mechanisms enhanced microwave response.

ARTICLE INFO

ABSTRACT

Constructing different 2D nano-materials into hybrids is an effective way to fabricate high-performance microwave absorbing (MA) materials. The formed heterointerfaces offers new loss mechanisms to make up the shortages of sole material in attenuating electromagnetic energy. For practical utilizations, microwave absorbers perform at low-frequency band with light-weight and thinness are more desirable. Here, hybrids aerogel microspheres constructed from graphene oxide (GO) and Ti$_3$C$_2$T$_x$ MXene are manufactured by rapid freezing assisted electrostatic-spinning. Combined with the disparities of conductivity between Ti$_3$C$_2$T$_x$ MXene and GO, and the newly generated heterointerfaces and abundant surface groups, the Ti$_3$C$_2$T$_x$ MXene@GO hybrid aerogel microspheres (M@GAMS) exhibit optimized impedance matching and improved MA performance. Besides, the unique aerogel structure not only offers light weight merit for this absorber but also elongates the attenuating paths when electromagnetic waves inject in. With a rather low filler loading of 10.0 wt% and a thickness of 1.2 mm, the optimized M@GAMS exhibit reflection loss (RL) of -49.1 dB at 14.2 GHz. More importantly, the M@GAMS present effective MA at S-band, and the RL reaches -38.3 dB at 2.1 GHz with a thickness of 5.0 mm. We believe the M@GAMS provides new opportunities for designing efficient MA absorbers, especially for the low-frequency.

1. Introduction

In the electromagnetic protection field, graphene and its derivates have tremendous advantages owing to their high dielectric loss capability, light weight and modifiability [1,2]. While pristine graphene suffers from limited loss mechanisms and serious impedance mismatching caused by improper electrical conductivity, it is mainly applied in electromagnetic interface shielding. Graphene oxide (GO) has more loss mechanisms, however, poor conductive loss mechanism hinders the ability of attenuating electromagnetic waves. Generally, reduced GO is more popular in microwave absorption (MA) field for the

proper impedance matching, abundant loss mechanisms and dielectrical loss ability, but still limited by its high costs and complicated processing [3].

Assembling 2D graphene layers into 3D structures, like aerogels and foams, is a practical way to improve their MA ability by elongating the reflecting and scattering paths to microwaves, generating new interfaces and adjusting the impedance matching [4,5]. When microwaves shoot into the 3D structure, the cell walls greatly shorten the impedance gap with free space and weaken reflection and scattering from adjacent cell walls and struts, which helps improving the MA performance [6]. GO is the most common graphene derivate used to fabricate 3D

structure, owing to the chemical reactivity [7]. To pursue greater MA performance, conductive or magnetic components were often employed in GO, which needs further reduction to achieve efficient carrier transport at the interface [8]. Yet, it remains challenging to achieve a high-performance MA of the GO-based composites with facile route. $Ti_3C_2T_x$ MXene, a kind of flexible 2D material that attracted much attention in MA field due to its varieties of remarkable properties, including light weight, high conductivity and highly active surface property, especially the abundant functional groups on the surface enabling it to be modified with other materials without the expense of intrinsic property and structural destruction [9,10]. In light of moderate dielectric constant and active surface characteristics, $Ti_3C_2T_x$ MXene has been considered as a potential dielectric mediator in GO-based hybrid to shield or absorb electromagnetic waves [11,12]. A 3D hybrid composed of GO and $Ti_3C_2T_x$ MXene would rely on both the intrinsic properties of 2D materials and the unique advantages of microstructures to gain a remarkable MA performance due to the moderate dielectric loss ability and optimized impedance matching brought by the newly generated heterogeneous interfaces and hierarchical porous structures.

Herein, we demonstrate, for the first time, the construction of $Ti_3C_2T_x$ MXene@GO hybrid aerogel microspheres (M@GAMS) by integrating GO with $Ti_3C_2T_x$ MXene *via* electrostatic-spinning technique strategy assisted with rapid freezing and freeze drying. Driven by the hydrogen bonding interactions, GO and $Ti_3C_2T_x$ MXene layers are ingeniously assembled into heterogeneous structures with a face-to-face form. This hybrids exhibit good MA performance in 2–18 GHz, it achieves the minimum reflection loss of − 49.1 dB at 14.2 GHz with a thickness of 1.2 mm. More importantly, the M@GAMS has also excellent MA performance at S-band. The newly generated interfaces, special spatial structure and the presence of highly conductive $Ti_3C_2T_x$ MXene are thought to be the main reasons behind the impressive MA performance of this GO-based material.

2. Material and methods

2.1. Preparation of $Ti_3C_2T_x$ MXene@GO aerogel microspheres

The $Ti_3C_2T_x$ MXene and GO are prepared by the typical etching method with HCl and LiF and modified Hummers method [13,14], respectively. The layered structure of GO and $Ti_3C_2T_x$ MXene was recorded by an atomic force microscope (AFM), as shown in Fig. S1, from which it can be seen that the thicknesses of GO and $Ti_3C_2T_x$ MXene are both in 1–3 nm, indicating the number of layers is less than 10 of GO and a single layer of $Ti_3C_2T_x$ MXene. Typically, to fabricate M@GAMS with MXene fraction of 30 wt%, 3.5 mL GO precursor (12 mg/mL) was added into the 3.6 mL of $Ti_3C_2T_x$ MXene solution (5 mg/mL) and 2.9 mL ultrapure water with a dropper and stirred for 5 min. Then, the mixture was sucked into a polypropylene syringe, after which the spinning process was started immediately under a voltage around 5 KV with an injection rate of 0.08 mL per minute. At the same time, a Dewar bottle filled with liquid nitrogen (−196 °C) was used as the collector below the end of the syringe needle for the micro-droplets resulting from the electrospun dispersion. Then, the droplets would be frozen immediately when dropt from the needle. The frozen droplets were collected and dried under a vacuum freezing dryer for 2 days. By changing the $Ti_3C_2T_x$ MXene fracture in mixture, a series of M@GAMS were obtained and denoted as X_M = fraction of $Ti_3C_2T_x$ MXene (5, 10, 15, 30, 35, 45, 50, 70, 80), while the pure GO and $Ti_3C_2T_x$ MXene were named as GAMS and MAMS, respectively.

2.2. Characterization

X-ray diffraction patterns were recorded with a X-ray diffractometer (XRD, X-30, Philips, Dutch) with Cu Kα radiation (λ = 1.54056 Å). Scanning electron microscope (SEM, JSM-7800F, JEOL, Japan) and

transmission electron microscope (TEM, JEM-2100, JEOL, Japan) were used to characterize the morphology, microstructure and elemental mapping of $Ti_3C_2T_x$ MXene, GO and $Ti_3C_2T_x$ MXene@GO aerogel microsphere. X-ray photoelectron spectra (XPS) measurements were carried out using Thermo Scientific ESCALAB 250Xi which is equipped with a hemispherical electron analyzer and Al Kα X-ray source. Raman spectra were conducted on an InVia Reflex (Renishaw, England) with an excitation wavelength of 532 nm. Fourier Transform Infrared Spectroscopy (FT-IR, Tensor II, Bruker, USA) was conducted with spectral resolution of $2 \, cm^{-1}$. Atomic Force Microscope (AFM, CSPM5500, Benyuan, China) was used to measure the lateral size of $Ti_3C_2T_x$ MXene and GO. A Leica DM6000 FS was applied to check the structural integration of microspheres after the specific process of microwave test was determined. The electromagnetic parameters of the frequency range of 0.5–18 GHz were collected by the vector network analyzer (VNA, 15071C, Agilent, America) through the coaxial-line method. The testing samples were prepared by filling the wax into the aerogel microspheres with a weight ratio of 1:9 toroidal-shaped samples (Φout = 7.00 mm, Φin = 3.04 mm), the shape of M@GAMS is well preserved (Fig. S11). The RL values were calculated by Eqs. (1) and (2).

3. Results and discussion

3.1. Structural analysis

In the electrospinning process, the liquid is stretched at the tip end into a "*Taylor cone*", and a spherical droplet will break away at a certain voltage level [15]. The droplets are immediately frozen in a liquid nitrogen bath and dried in a vacuum drier for preparing M@GAMS, based on the hydrogen bonds among GO and MXene sheets and the interations during the process of rapid freezing with growing ice fronts [11]. The hydrogen bonds make GO and MXene layers attractive to form hybrid assemblies, which then be repulsed or entrapped by the moving ice-fronts and be concentrated at crystal boundaries to form 3D networks [16,17]. After removing of ice crystals, the 3D network is obtained. Scanning electron microscopy (SEM) images (Figs. 1 and S2) show that all the as-obtained aerogel microspheres exhibit the uniform size (mean diameter ∼500 μm), except for some small microspheres which generates from the splashed beads from needle during spinning. Interestingly, the addition of $Ti_3C_2T_x$ MXene affects the size and cell shape of the pore structure (Fig. 1a–c). For the pure graphene oxide aerogel microspheres (GAMS) (Fig. 1a), the pores are randomly interconnected and the cell walls are wrinkled, while when adding $Ti_3C_2T_x$ MXene into GO to achieve M@GAMS (X_M is denoted as the fraction of $Ti_3C_2T_x$ MXene), the pores turns regular and the cell walls become more straight (Figs. 1b–1c and S3), and when there is only $Ti_3C_2T_x$ MXene (MAMS), the cell walls are rough and slightly crumpled (Fig. 1c). The differences are arisen by the difference in the rigidity of the GO and MXene layers, the more rigid MXene layers act as a scaffold to restrain the crimping of GO layers in the integrations. Besides, the layer size of GO and MXene layers differs a lot, large GO layers and M@GAMS assemblies could act as a single wall for a cell, while for MAMS a cell wall must be constructed from many MXene layers, this also makes the cell wall MAMS rough and crumpled during freezing [18]. This well-constructed 3D hybrid structure that helps to enhance the mechanical strength of M@GAMS and protect it against deformation during processing.

To figure out the assembly structure of GO and $Ti_3C_2T_x$ MXene in hybrids, transmission electron microscope (TEM) and high resolution TEM (HRTEM) are applied. A compact stacking structure containing $Ti_3C_2T_x$ MXene and GO layers is observed, as shown in Fig. 2a–b, besides, the layer spacing of crystal $Ti_3C_2T_x$ MXene is enlarged from 0.24 nm to 1.23 nm due to the existence of GO layers (Fig. S4), which proves that this stacking structure is a mutually stacking structure with a face-to-face form. This face-to-face form was proved to be beneficial to protect MXene from oxidizing, due to the large GO layers could warp MXene layers to be isolated from the air [12,16]. Moreover, the element
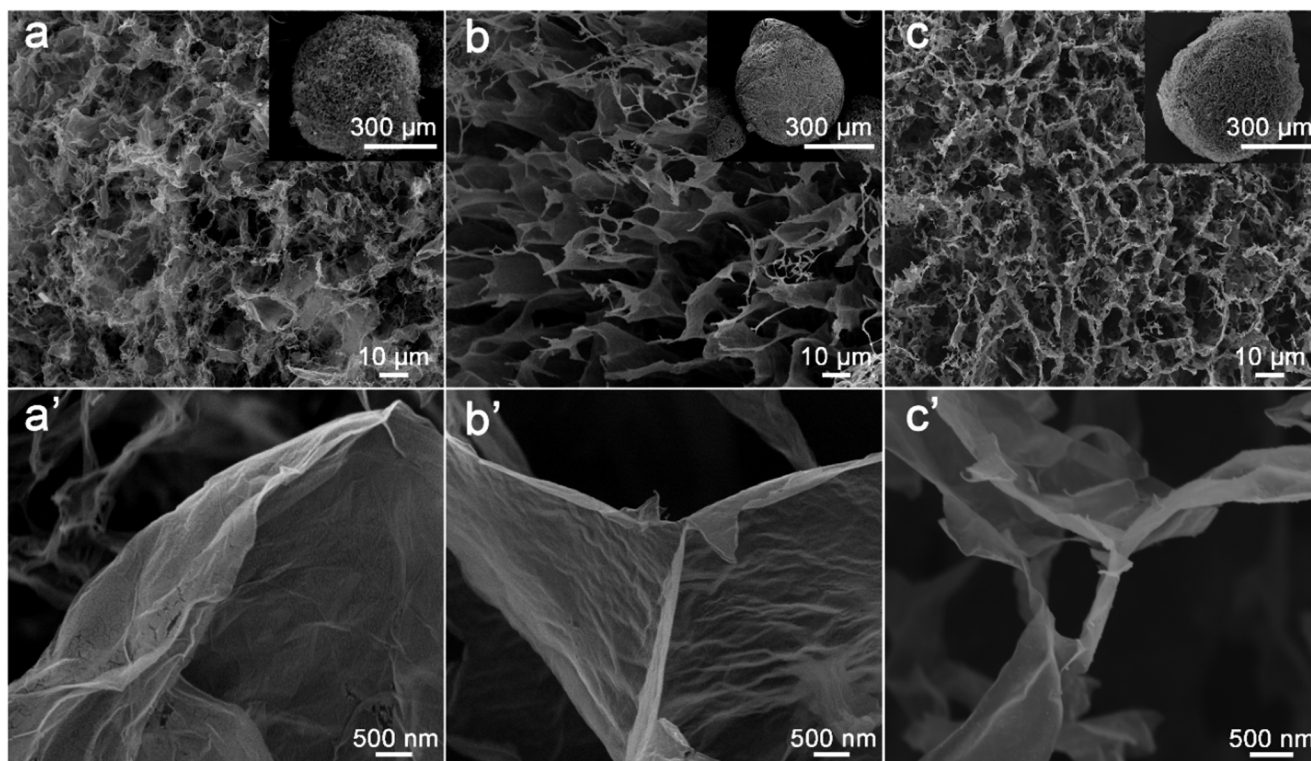
Fig. 1. Morphological characterization of hybrid aerogels. SEM images of the as-prepared aerogels (a) GAMS, (b) M@GAMS with $X_M = 30$ and (c) MAMS. The inserts are the overall view of the corresponding aerogels, and the (a′)–(c′) are the details corresponding to (a)-(c) with high magnification, respectively.

mapping analysis of cell walls indicates a uniformly assembled structure of M@GAMS (Fig. 2d–g). As for the atomic ratio, the calculated atomic ratio of Ti/C in the M@GAMS with $X_M = 30$ is about 3/14, far less than that of MAMS (about 5/6) (Fig. S5). The excess proportions should be ascribed to the existence of GO. These further prove that this stacking assembly is a hybrid structure composed of GO and $Ti_3C_2T_x$ MXene.

The structure of M@GAMS is further confirmed by X-ray diffraction

(XRD), X-ray photoelectron spectrum (XPS), FT-IR and Raman spectra. The XRD patterns (Fig. 3a) show that, after addition of $Ti_3C_2T_x$ MXene with X_M lower than 10, both the peaks at 9.96° and 6.63° respectively belonging to GO (0 0 1) and $Ti_3C_2T_x$ MXene (0 0 2) exist [9,19], but disappear when the X_M is above 10. While a new peak appears in case of X_M higher than 10, this peak should be described to the hybrids that are assembled by stacking GO and $Ti_3C_2T_x$ MXene layers. It can be found that this peak shifts from 6.65° to 7.93° along with the increasing of X_M
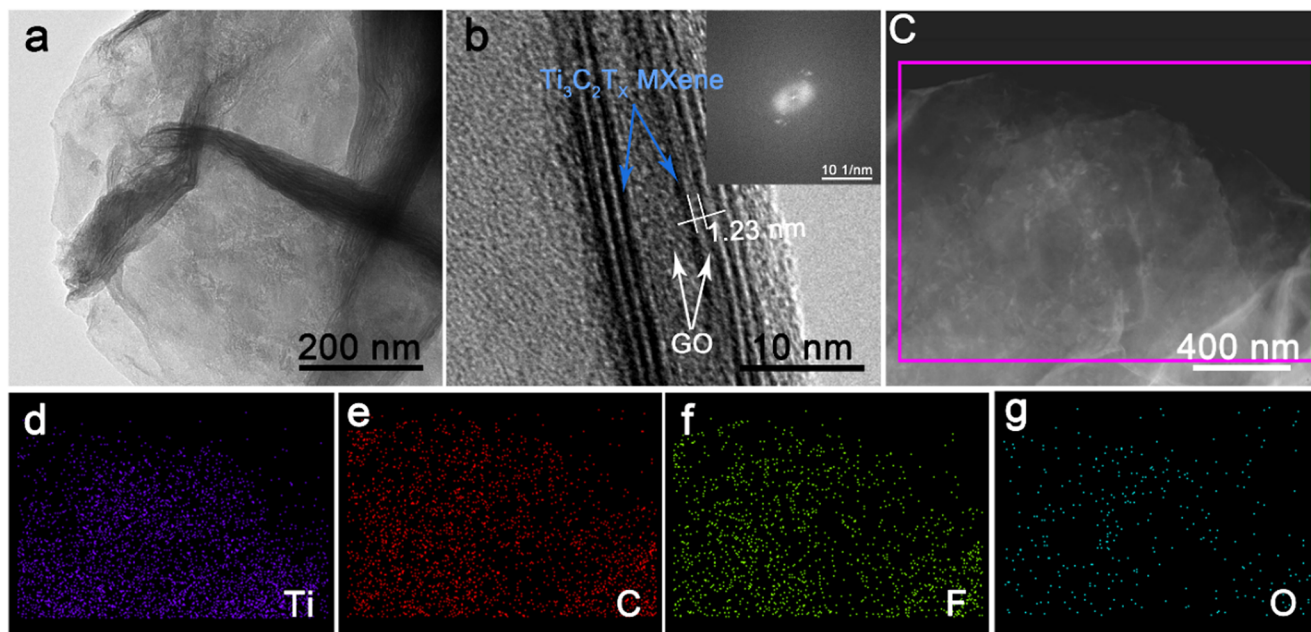

Fig. 2. Structural analyses of hybrid aerogels. (a) TEM images of M@GAMS ($X_M = 30$) and (b) the corresponding high-magnification images. (c) The selected region and result of M@GAMS for elements distribution analysis, (d-g) the distribution mappings of Ti, C, F and O, respectively.
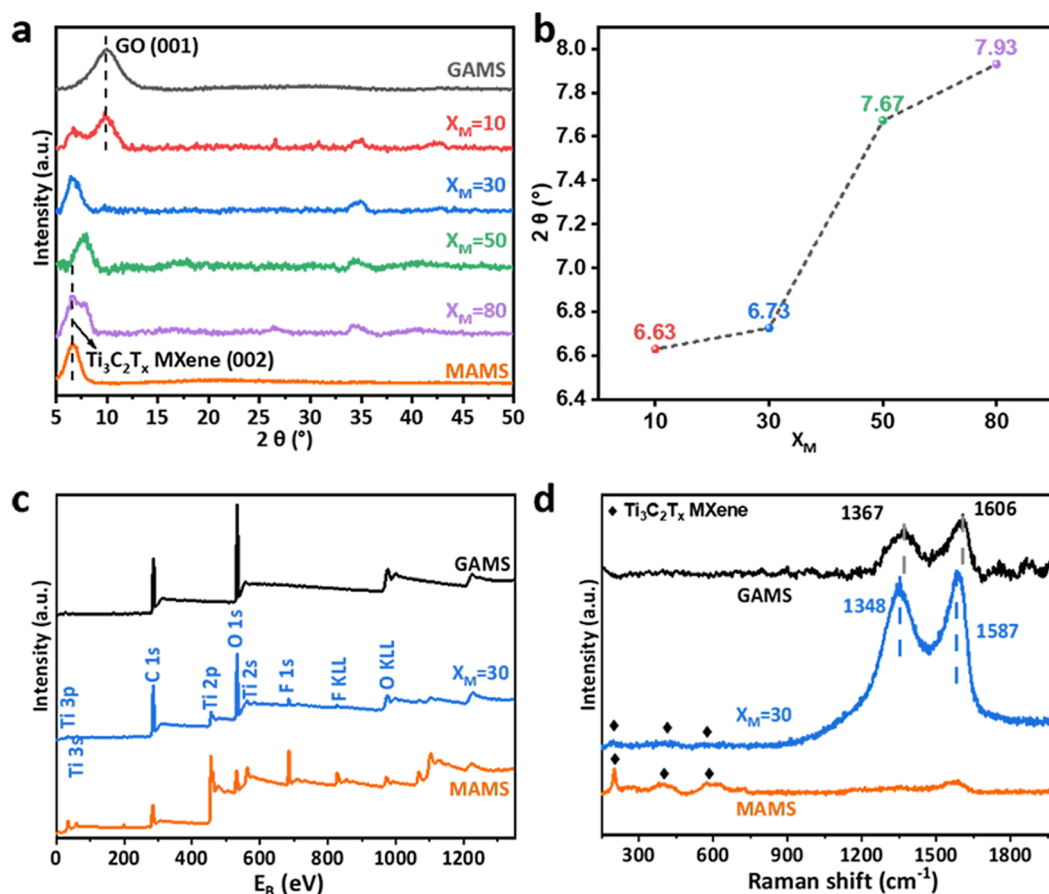
Fig. 3. Structural analysis of hybrid aerogels. (a) XRD patterns, (b) the peak shifts of M@GAMS with X_M, (c) the full XPS spectrum and (d) the Raman spectrum of GAMS, M@GAMS ($X_M = 30$) and MAMS.

(Fig. 3b), which corresponds to a shrinkage of interlayer space from 13.33 Å to 11.15 Å (Fig. S6) owing to the formation of stacking structure induced by intercalation of GO in MXene [10]. When X_M goes up to 80, the $Ti_3C_2T_x$ MXene (0 0 2) appears again, which results from the coexistence of the formed hybrid and excessive $Ti_3C_2T_x$ MXene. Besides, the XPS and Raman results further demonstrate the integration of hybrids. Firstly, there exist C, O, Ti and F in M@GAMS with $X_M = 30$ in XPS spectra (Fig. 3c). Secondly, the bonding energies of both C-OH, C=O and C-O-C in GO and C-C, Ti-C-O, C-F, Ti-C and C-O in $Ti_3C_2T_x$ MXene with $X_M = 30$ have a downshift and upshift respectively, implying the interactions between GO and $Ti_3C_2T_x$ MXene layers (Fig. S9a–c) [20]. Also, the shift of C-OH bond from 3424 cm^{-1} to 3418 cm^{-1} in the FT-IR spectra proves the existence of hydrogen bond interactions (Fig. S7) [12]. Thirdly, specific peaks of graphite structure (D band and G band) at 1348 and 1587 cm^{-1}, and peaks of $Ti_3C_2T_x$ MXene around 200 and 400 cm^{-1} can be found simultaneously (Fig. 3d, S8). What's more, the peak of D and G bands broadens after integration and the I_D/I_G ratio increases from 1.24 to 1.32, which further substantiates that the addition of $Ti_3C_2T_x$ MXene affects the structure of GO and the integrated hybrids [21].

Based on the above discussions, the assembly mechanism of M@GAMS is be described as Fig. 4. Firstly, the GO and $Ti_3C_2T_x$ MXene layers are assembled spontaneously into hybrids by hydrogen bonding interactions, after which the liquid is stretched into spherical droplets at the needle end of electrostatic spinning. Then the acquired droplets fell into the liquid N_2 in the Dewar bottle, thus were frozen immediately. During the freezing process, the formed assemblies are gathered at the ice boundaries and squeezed by the moving ice fronts, which start from the droplets surface to the core, and thus the 3D network is obtained after removing the ice by freeze drying. The

interlayer space is affected by the proportion of $Ti_3C_2T_x$ MXene due to the various stacked structures of hybrid assemblies, so the layered structure of M@GAMS can be easily adjusted.

3.2. Microwave absorption

The electromagnetic parameters in the frequency range of 2.0–18.0 GHz were collected by the vector network analyzer through the coaxial-line method, and the RL values were calculated from Eqs. (1) and (2), where Z_{in} is the input characteristic impendence, Z_0 the free space impendence, μ_r and ε_r the measured complex permeability and complex permittivity, d the thickness of tested sample, c the propagation velocity of microwave in free space and f the frequency of microwave. Besides, the permeability was taken as 1 due to the nonmagnetic properties of M@GAMS.

$$RL = 20 \lg \left| \frac{(Z_{in} - Z_0)}{(Z_{in} + Z_0)} \right| \tag{1}$$

$$Z_{in} = Z_0 \sqrt{\mu_r / \varepsilon_r} \tanh \left[j (2\pi f d / c \sqrt{\varepsilon_r \mu_r}) \right] \tag{2}$$

As shown in Fig. 5, the pristine GAMS and MAMS barely meet the efficient absorption of −10.0 dB (Fig. 4a and insert), while integrating GO with $Ti_3C_2T_x$ MXene in the form of aerogel microspheres can significantly enhance its MA capacity. In case of $X_M = 10$, the minimal RL (RL_{min}) reaches −26.7 dB at 16.9 GHz with thickness of 2.0 mm, and the bandwidth of RL < −10 dB is 1.5 GHz (from 16.5 to 18.0 GHz) (Fig. 5b). The MA performance can be optimized, on condition that $X_M = 30$, RL_{min} value of −49.1 dB at 14.2 GHz with a thickness of 1.2 mm is reached and the corresponding bandwidth of RL < −10.0 dB is 2.9 GHz (from 12.9 to 15.8 GHz) (Fig. 5c). Interestingly, the effective
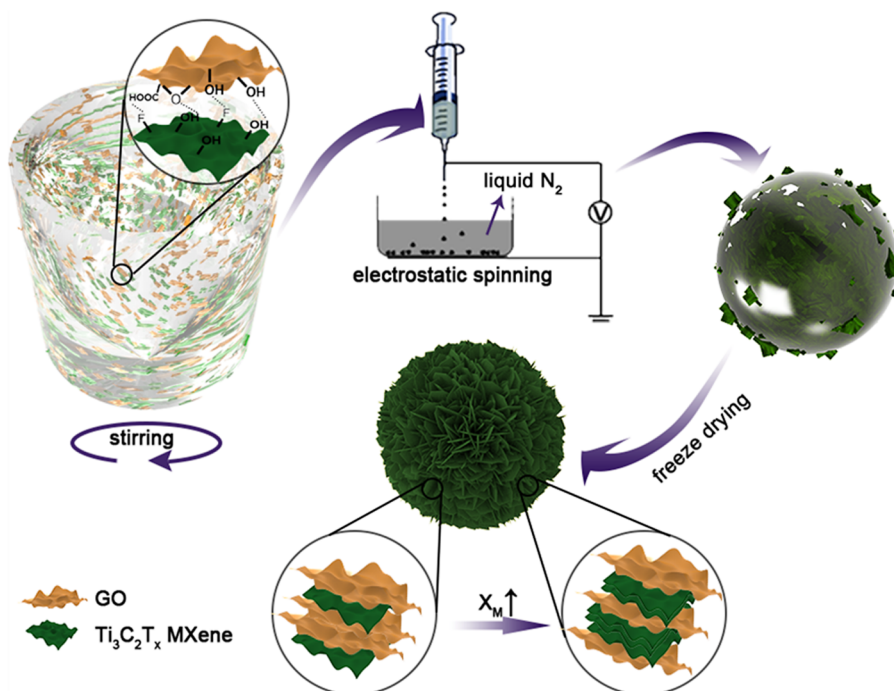
Fig. 4. The assembly mechanism of M@GAMS during processing.

bandwidth shifts to low-frequency band with the increase of X_M. For $X_M = 50$, the effective absorption with RL below -10.0 dB covers the whole S band by adjusting the thickness from 4.5 to 5.0 mm (Fig. 5d). This indicates a positive contribution of MXene to GO-based material in MA performance. However, as the X_M continues to increase, the MA capacity gradually decreases and when X_M increases up to 80, the RL_{min} is only -12.5 dB at 2.0 GHz with thickness of 5.0 mm (Fig. 5e). This is because the excess $Ti_3C_2T_x$ MXene causes the impedance mismatching (details are given below). Furthermore, Fig. 5f shows the RL_{min} values

of M@GAMS with different X_M ranging from 2.0 to 4.0 GHz, and it can be seen that the hybrid aerogel microspheres also present effective MA capacity at S band, such as the RL_{min} of $X_M = 70$ reaches -38.3 dB at 2.1 GHz with a thickness of 5.0 mm. It is of significant benefit to low-frequency electromagnetic interference from the most electronic devices [22]. To further evaluate the MA performance of M@GAMS, the RL characteristics of typical MXene-based composites reported in the recent literature are summarized in Table 1. It can be found that the combination of GO and MXene with the lowest loading exhibits a
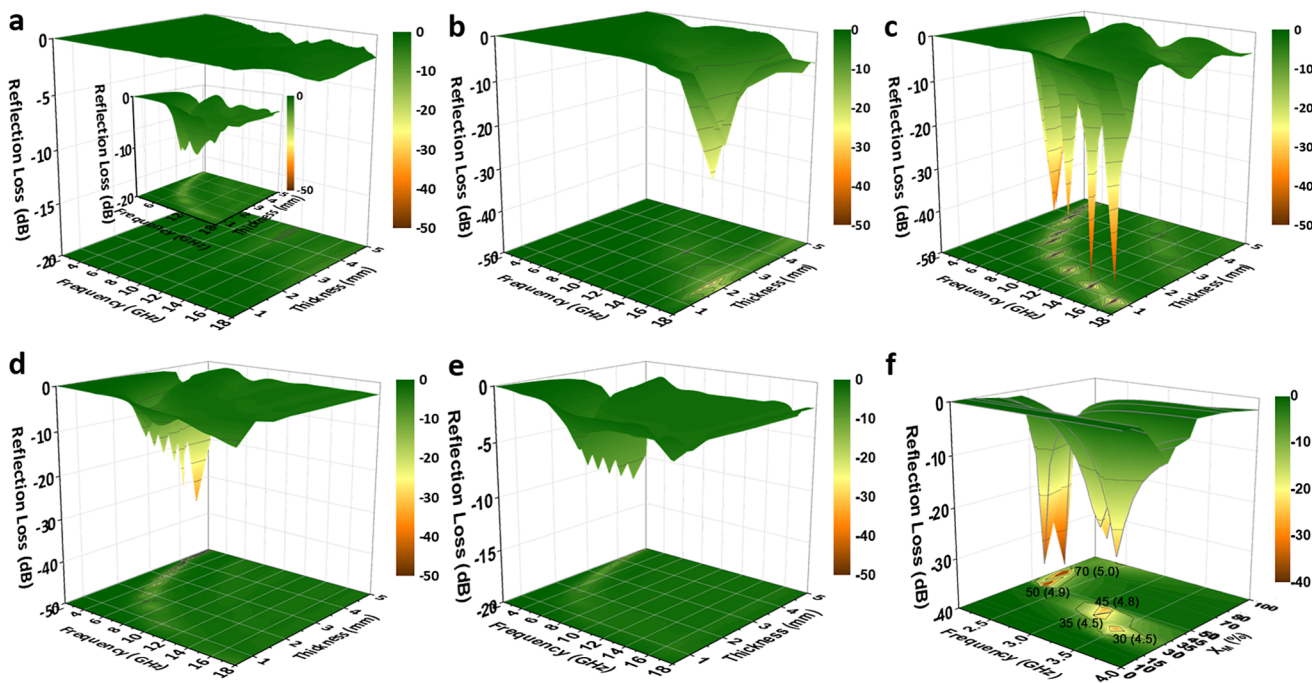

Fig. 5. The calculated reflection loss of GAMS and MAMS (a), and M@GAMS with X_M of 10 (b), 30 (c), 50 (d) and 80 (e) with thickness of 0.5–5.0 mm, (f) the reflection loss at S band for M@GAMS with different X_M, the thickness are listed in brackets.

Table 1
Microwave absorption performance of MXene-based composites.

Filler	Loading (wt%)	RL$_{min}$		Effective absorption		Ref.
		Value (dB)	Thickness (mm)	Band width (dB)	Thickness (mm)	
Ti$_3$C$_2$T$_x$ MXene	55	−30.0	1.8	2.8	1.4	[6]
Ti$_3$C$_2$T$_x$/PPy[a]	25	−49.2	3.2	4.9	3.2	[20]
Graphite/TiC/Ti$_3$C$_2$	50	−63	2.1	3.5	2.1	[23]
Ti$_3$C$_2$T$_x$ MXene/cellulose aerogel	24	−43.4	2	4.5	2	[24]
Ti$_3$C$_2$T$_x$ MXene/nano-carbon-sphere	50	−54.67	4.8	–	–	[25]
Ti$_3$C$_2$T$_x$/CNT	35	−52.9	1.55	4.46	1.55	[26]
Ti$_3$C$_2$/FCI[b]	60	−15.5	1.0	8.16	1.0	[27]
MXene/PI[c] aerogel	–	−45.4	3	3.7	3	[28]
RGO[d]/Ti$_3$C$_2$T$_x$ hybrids foam	–	~ −22	3.6	4	3.2	[12]
M@GAMS	10	−49.1	1.2	2.9	1.2	This work

[a] polypyrrole,
[b] flaky carbonyl iron,
[c] polyimide,
[d] reduced graphene oxide

superior RL$_{min}$ at a very small thickness. This result implies the promising perspective of M@GAMS in the development of light microwave absorber.

The MA performance is closely related to the electromagnetic parameters, the complex permittivity and loss tangent $tan\delta$ (calculated by Eq. (3)) of M@GAMS/wax composites with different X_M are measured and shown in Fig. 6. ε' represents the dielectric and polarization property of material, and an increase indicates that the material is easier to be polarized under the action of an external magnetic/electrical filed. The frequency dependence of ε' for M@GAMS is shown in Fig. 6a, and it can be seen that the ε' trends to decrease along with the increases in frequency, which can be comprehended by the increased lagging of polarization with respect to electric-field change at higher frequency [29,30]. Besides, the ε' of all samples increase along with the increasing of X_M due to the contribution of high conductivity of Ti$_3$C$_2$T$_x$ MXene. While for MAMS, the decrease of heterointerface weaks its ability of dielectric and polarization, leading to the decrease of ε'. ε'' stands for the dielectric loss of materials. As depicted in Fig. 6b, ε'' increases along with the increase of X_M, demonstrating that the increase in Ti$_3$C$_2$T$_x$ MXene is beneficial to electromagnetic wave loss. The $tan\delta$ of M@GAMS with the increase of X_M is displayed in Fig. 6c, which also embodies a strong dependence on X_M, indicating the significant attribution of Ti$_3$C$_2$T$_x$ MXene to convert electromagnetic wave energy into other forms of energy [31]. The above results shows that the addition of Ti$_3$C$_2$T$_x$ MXene affects the electromagnetic parameters of M@GAMS, highlighting the crucial contribution of Ti$_3$C$_2$T$_x$ MXene to the functionality of M@GAMS. The change of dielectric loss mechanism aroused by addition of Ti$_3$C$_2$T$_x$ MXene can be addressed by Cole-Cole circles. The dielectric loss mainly involves electron polarization, ion polarization and electric dipolar polarization, and the former two are relatively weaker in the microwave range. Therefore, the electric dipolar polarization is a major contributor to dielectric loss, and its relaxation processes can be described by Cole-Cole semicircles based on the Debye dipolar relaxation:

$$tan\delta = \frac{\varepsilon''}{\varepsilon'} = \frac{(\varepsilon_s - \varepsilon_\infty)\omega\tau}{\varepsilon_s + \varepsilon_\infty \omega^2 \tau^2} \tag{3}$$

$$\varepsilon_s = \varepsilon' - j\varepsilon'' = \varepsilon_\infty + \frac{\varepsilon_s - \varepsilon_\infty}{1 + j2\pi f\tau} \tag{4}$$

where ε_s is the static dielectric constant, ε_∞ refers to the dielectric constant at infinite frequency, and τ indicates polarization relaxation time, respectively. The ε' and ε'' can be expressed as the following formulas.

$$\varepsilon' = \varepsilon_\infty + \frac{\varepsilon_s - \varepsilon_\infty}{1 + (j2\pi)^2 \tau^2} \tag{5}$$

$$\varepsilon'' = \frac{2\pi f\tau(\varepsilon_s - \varepsilon_\infty)}{1 + (j2\pi)^2 \tau^2} \tag{6}$$

From the above equations, the relationship between ε' and ε'' can be deduced as the following expression [32].

$$\left(\varepsilon' - \frac{\varepsilon_s + \varepsilon_\infty}{2}\right)^2 + (\varepsilon'')^2 = \left(\frac{\varepsilon_s + \varepsilon_\infty}{2}\right)^2 \tag{7}$$

Each semicircle represents a Debye relaxation process, and the semicircles for all the M@GAMS are depicted in Fig. 6d, implying the presence of multi-dielectric relaxations (the enlarged Figures of GAMS and $X_M = 10$ are shown in Fig. S9). The abundant heterointerface formed by GO and Ti$_3$C$_2$T$_x$, and defects, such as boundaries, stacking faults and surface functional groups, are further contributed to enhance the relaxation processes. Moreover, the numbers of semicircles for GAMS and MAMS are less than that of M@GAMS, which emphasizes the relaxation processes mainly caused from the interface between GO and Ti$_3$C$_2$T$_x$ MXene layers (Fig. 6g). For M@GAMS, there exist the same number of semi-circle but in different positions and radiuses. With increasing of X_M, the semi-circles moves to higher position and the radiuses increases simultaneously, implying higher polarization ability of M@GAMS with higher X_M [33]. Furthermore, there exists about six kinds of relaxation processes in hybrids, just like the enlarged view of $X_M = 30$ (Fig. 6e). The semicircle I represents the high-frequency structural resonance caused by layer-stacked structure in M@GAMS hybrids [34], and II–V indicates the polarization relaxations and interfacial polarization loss, which are the polarization of Ti$_3$C$_2$T$_x$ MXene and GO layers caused by surface groups and defects at external electromagnetic field, spatial polarization at hybrids interfaces aroused by different induced charges' moving velocity on Ti$_3$C$_2$T$_x$ MXene and GO layers, new polarization centers caused by the accumulation of charge at interfaces and amorphous carbon on partially oxidized Ti$_3$C$_2$T$_x$ MXene layers [10,23,35]. In addition, the conductivity is another important factor that contributes to the dielectric loss of M@GAMS. The circle VI attributed to conductivity confirms the increasing conductive loss owing to the addition of high-conductive Ti$_3$C$_2$T$_x$ MXene [3,36–38].

In addition, the contribution to dielectric loss can be calculated based on Debye Theory. The complex component including relaxation and conductance is calculated by Eq. (8).

$$\varepsilon''(\omega) = \varepsilon_p'' + \varepsilon_c'' = (\varepsilon_s - \varepsilon_\infty)\frac{\omega\tau}{1 + \omega^2 \tau^2} + \frac{\sigma}{\varepsilon_0 \omega} \tag{8}$$

where σ is electrical conductivity and ω the angular frequency. Based on the theory, the ε'' can be classified as ε_p'' induced by relaxation and ε_c'' generated from conductance. The τ, σ, polarization loss and conductive loss are fitted by non-linear square fitting mode (see details in
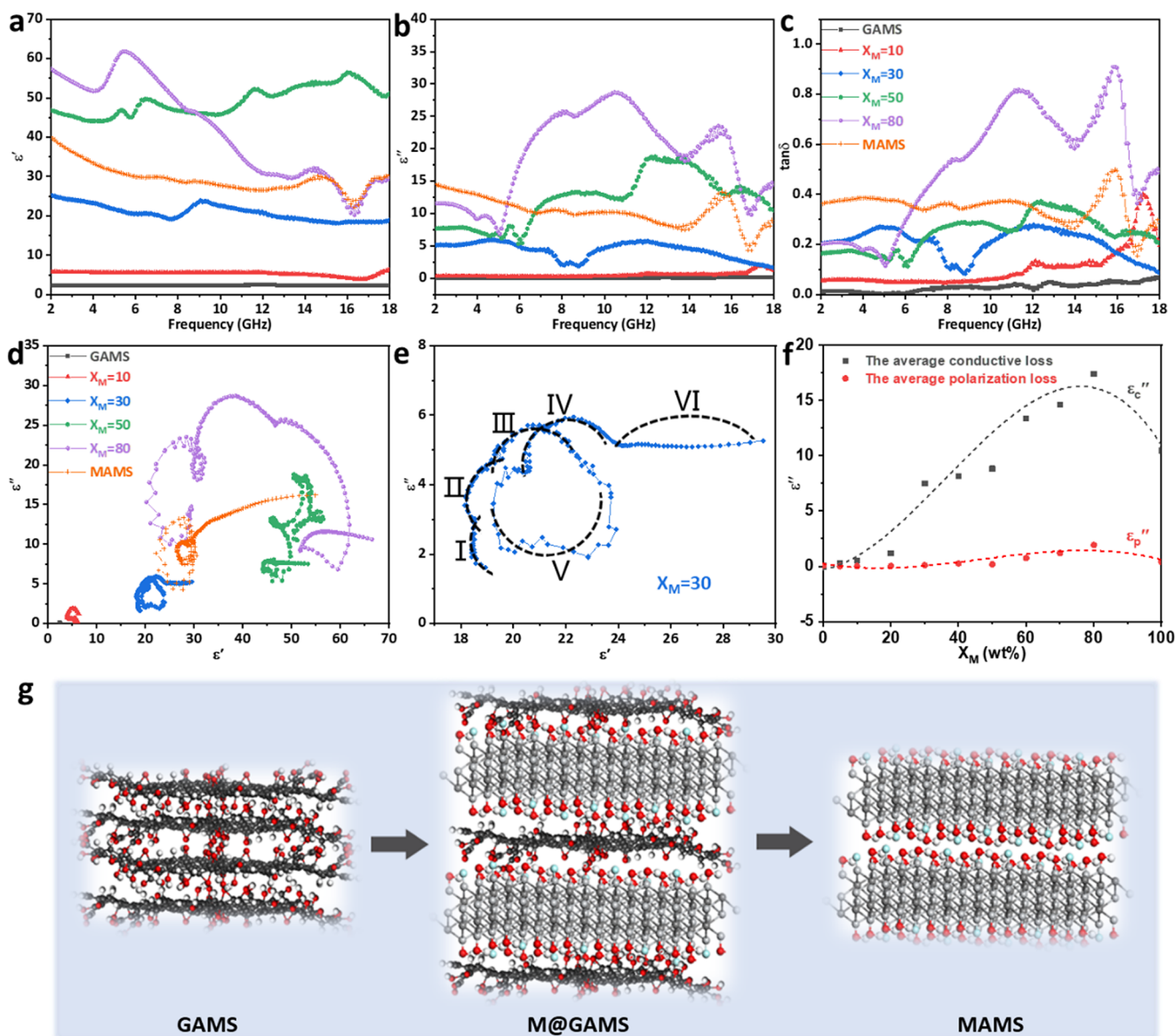
Fig. 6. Measured frequency dependence of (a) ε', (b) ε'', (c) *tanδ* of GAMS, MAMS and M@GAMS with X_M of 10, 30, 50 and 80. (d) Cole-cole curves of GAMS, MAMS and M@GAMS with X_M of 10, 30, 50 and 80, (e) the enlarged version of $X_M = 30$, (f) the fitted averages of ε_c'' and ε_p'' versus X_M of M@GAMS and (g) the schematic illustration of interfaces in GAMS, MAMS and M@GAMS.

supporting information) [39]. As presented in Figs. 6f and S10, on the whole, ε_c'' is higher than ε_p'' in ε'' due to the formation of conductive network in wax matrix, which could cause high conductive loss [32,40]. Thus, the contribution of ε_c'' to ε'' is significantly higher than that of ε_p''. Furthermore, the average ε_c'' dramatically increases along with the addition of conductive $Ti_3C_2T_x$ MXene. Due to the fact that the disappearance of heterointerface in MAMS will lead to the reducing of induced eddy current, the intrinsic ε_c'' of MAMS (Figs. 6f and S10f) shows an obvious drop, compared to M@GAMS with $X_M = 80$.

Excellent MA performance should be obtained only when the material possesses both loss characterizations and impedance matching [41,42]. To explain the superior MA performance under $X_M = 30$ to the others, firstly, the loss characterization (attenuation constant, α) is evaluated by Eq. (9) (Fig. 7a). It can be found that α increases as X_M goes up in the whole range of 2–18 GHz except a drop at MAMS, implying that adding $Ti_3C_2T_x$ MXene into hybrids is beneficial to the loss of microwaves while the the loss ability of pristine MXene is relatively weaker than hybrids with $X_M = 50$ and 80. Secondly, the impedance matching degree (delta, Δ) is evaluated by Eq. (10), in which the K and

M can be calculated from the relative permittivity and relative permeability by Eqs. (11) and (12) [43,44]. According to the impedance matching theory, the impedance matching degree should be equal or close to that of free space at the interfaces between absorbers and free space. Impedance mismatching would cause reflection or transmission of most electromagnetic waves, and a Δ value smaller than 0.2 is considered acceptable for MA performance. For M@GAMS, the formation of hybrid improves the impedance matching of pristine GO and the porosity generated in the processes of electrostatic spinning and freeze drying effectively affects its dielectric properties, and further helps to optimize the Δ. As presented in Fig. 7b–f and insert, the M@GAMS with $X_M = 30$ possesses the largest area of (Δ less than 0.2) over other M@GAMS, indicating its advantaged impedance matching degree over the others. The excellent impedance matching degree fits the above reflection loss results. In conclusion, the excellent MA performance of M@GAMS with $X_M = 30$ should be attributed to its optimized impedance matching and high attenuation ability.
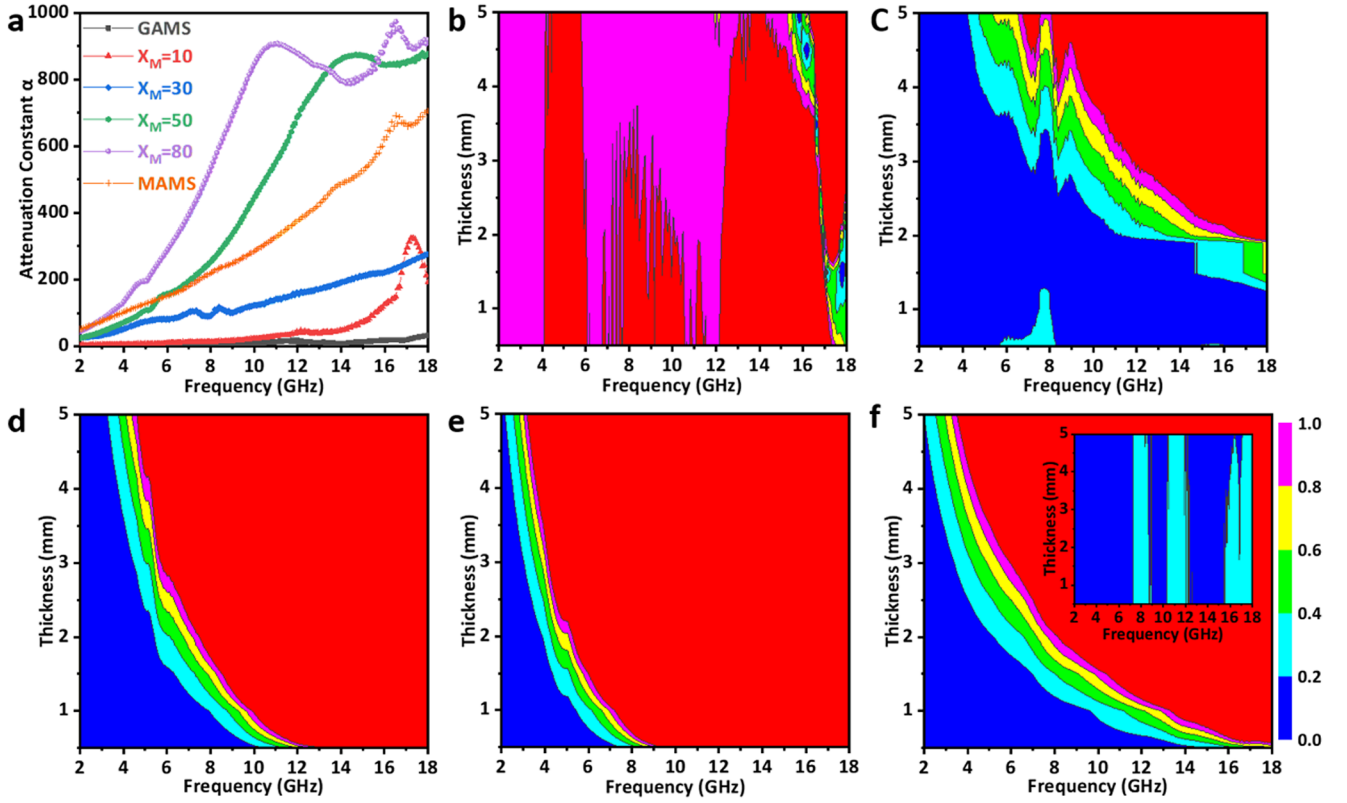
Fig. 7. The calculated attenuation constant of α (a), the calculated Δ value maps of M@GAMS with X_M of 10 (b), 30 (c), 50 (d), 80 (e), MAMS (f) and GAMS (insert in f) with thickness of 0.5–5 mm.
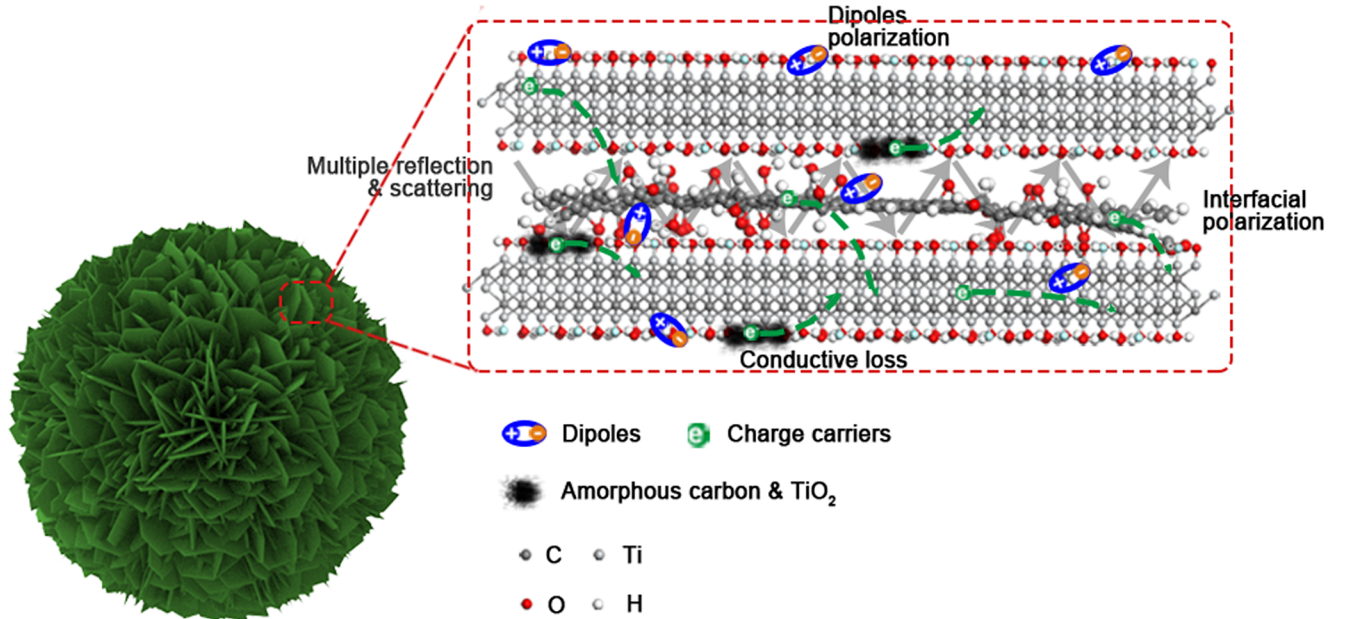

Fig. 8. Schematic illustration of the absorption mechanism of M@GAMS.

$$\alpha = \frac{\sqrt{2}\pi f}{c}\sqrt{(\mu^{\hat{E}°}\varepsilon^{\hat{E}°} - \mu'\varepsilon') + \sqrt{(\mu^{\hat{E}°}\varepsilon^{\hat{E}°} - \mu'\varepsilon')^2 + (\mu^{\hat{E}°}\varepsilon^{\hat{E}°} + \mu'\varepsilon')^2}} \tag{9}$$

$$\Delta = |\sinh^2(kfd) - M| \tag{10}$$

$$K = 4\frac{\pi\sqrt{\mu'\varepsilon'}\sin\left(\frac{\varepsilon+\mu}{2}\right)}{c\cdot\cos\varepsilon\cdot\cos\mu} \tag{11}$$

$$M = 4\frac{\mu'\varepsilon'\cos\varepsilon\bullet\cos\mu}{(\mu'\cos\varepsilon - \varepsilon'\cos\mu)^2 + \tan^2\left(\frac{\varepsilon-\mu}{2}\right)\bullet(\mu'\cos\varepsilon + \varepsilon'\cos\mu)^2} \tag{12}$$

Based on the above discussion, the MA mechanism of M@GAMS hybrids is proposed (Fig. 8). The addition of $Ti_3C_2T_x$ MXene significantly enhances the dielectric loss ability of GO-based hybrids by increasing the polarization capacity. The carriers migrate in the conductive $Ti_3C_2T_x$ MXene layers and hop to GO layers *via* the

heterointerfaces and defects, forming abundant field-induced micro-currents that gives rise to the conductive loss. The formed hybrids offer abundant heterointerfaces, defects such as boundaries, stacking faults and surface functional groups that enhances the polarization loss. Besides, by changing the fraction of $Ti_3C_2T_x$ MXene, the impedance matching can be optimized. Furthermore, the unique spatial structure of aerogel microspheres offer elongated reflecting and scattering paths to microwaves, which is also beneficial to the attenuation of microwave.

4. Conclusion

In summary, we synthesized a $Ti_3C_2T_x$ MXene@GO hybrid aerogel based on the rapid freezing assisted electrostatic spinning route. This hybrid possesses the following properties: (1) light, and porous to reduce the weight of electromagnetic wave absorbers in practical uses. (2) a new hybrid structure of face-to-face stacking form, which is easy to tune by changing the initial concentration of precursor in spinning solution. (3) high MA performance with RL of -49.1 dB to meet the practical requirements. (4) effective MA performance at 2–4 GHz to fill the gap of electromagnetic wave absorbers at S band. This route can massively prepare GO-based hybrid aerogel microspheres without reduction process to GO. The successful synthesis of such hybrids paves a way to expand the absorbing band of GO-based materials for not only C-Ku band but also S band with small thickness and low loading. Thus, this material has the potential to serve as electromagnetic wave absorber in the fields of arms, satellite and daily protection.

Acknowledgements

Appendix A. Supplementary data

Supplementary data to this article can be found online at https://doi.org/10.1016/j.cej.2019.123512.

References

[1] F. Meng, H. Wang, F. Huang, Y. Guo, Z. Wang, D. Hui, Z. Zhou, Graphene-based microwave absorbing composites: a review and prospective, Compos. B Eng. 137 (2018) 260–277.

[2] M. Bernardi, C. Ataca, M. Palummo, J.C. Grossman, Optical and Electronic Properties of Two-Dimensional Layered Materials, Nanophotonics 6 (2017).

[3] C. Wang, V. Murugadoss, J. Kong, Z. He, X. Mai, Q. Shao, Y. Chen, L. Guo, C. Liu, S. Angaiah, Z. Guo, Overview of carbon nanostructures and nanocomposites for electromagnetic wave shielding, Carbon 140 (2018) 696–733.

[4] H. Xu, X. Yin, M. Zhu, M. Li, H. Zhang, H. Wei, L. Zhang, L. Cheng, Constructing hollow graphene nano-spheres confined in porous amorphous carbon particles for achieving full X band microwave absorption, Carbon 142 (2019) 346–353.

[5] Y. Zhang, Y. Huang, H. Chen, Z. Huang, Y. Yang, P. Xiao, Y. Zhou, Y. Chen, Composition and structure control of ultralight graphene foam for high-performance microwave absorption, Carbon 105 (2016) 438–447.

[6] M. Han, X. Yin, X. Li, B. Anasori, L. Zhang, L. Cheng, Y. Gogotsi, Laminated and Two-Dimensional Carbon-Supported Microwave Absorbers Derived from MXenes, ACS Appl. Mater. Interfaces 9 (2017) 20038–20045.

[7] A. Arenillas, J.A. Menéndez, G. Reichenauer, A. Celzard, V. Fierro, F.J.M. Hodar, E. Bailón-Garcia, N. Job, Organic And Carbon Gels, Springer International Publishing, Switzerland, 2019.

[8] C. Wang, X. Han, P. Xu, X. Zhang, Y. Du, S. Hu, J. Wang, X. Wang, The electromagnetic property of chemically reduced graphene oxide and its application as microwave absorbing material, Appl. Phys. Lett. 98 (2011).

[9] C. Couly, M. Alhabeb, K.L. Van Aken, N. Kurra, L. Gomes, A.M. Navarro-Suárez, B. Anasori, H.N. Alshareef, Y. Gogotsi, Asymmetric Flexible MXene-Reduced Graphene Oxide Micro-Supercapacitor, Adv. Electron. Mater. 4 (2018) 1700339.

[10] F. Shahzad, M. Alhabeb, C.B. Hatter, B. Anasori, S. Man Hong, C.M. Koo, Y. Gogotsi, Electromagnetic interference shielding with 2D transition metal carbides (MXenes), Science 353 (2016) 1137–1140.

[11] S. Zhao, H.B. Zhang, J.Q. Luo, Q.W. Wang, B. Xu, S. Hong, Z.Z. Yu, Highly electrically conductive three-dimensional Ti3C2T x MXene/Reduced Graphene Oxide

[12] X. Li, X. Yin, C. Song, M. Han, H. Xu, W. Duan, L. Cheng, L. Zhang, Self-Assembly Core-Shell Graphene-Bridged Hollow MXenes Spheres 3D Foam with Ultrahigh Specific EM Absorption Performance, Adv. Funct. Mater. 28 (2018).

[13] M. Alhabeb, K. Maleski, B. Anasori, P. Lelyukh, L. Clark, S. Sin, Y. Gogotsi, Guidelines for Synthesis and Processing of Two-Dimensional Titanium Carbide (Ti3C2Tx MXene), Chem. Mater. 29 (2017) 7633–7644.

[14] Q. Yang, Y. Su, C. Chi, C.T. Cherian, K. Huang, V.G. Kravets, F.C. Wang, J.C. Zhang, A. Pratt, A.N. Grigorenko, F. Guinea, A.K. Geim, R.R. Nair, Ultrathin graphene-based membrane with precise molecular sieving and ultrafast solvent permeation, Nat Mater 16 (2017) 1198–1202.

[15] F. Meng, H. Wang, Z. Wei, T. Chen, C. Li, Y. Li, Z. Zhou Xuan, Generation of graphene-based aerogel microspheres for broadband and tunable high-performance microwave absorption by electrospinning-freeze drying process, Nano Res. 11 (2018) 2847–2861.

[16] Y. Yue, N. Liu, Y. Ma, S. Wang, W. Liu, C. Luo, H. Zhang, F. Cheng, J. Rao, X. Hu, J. Su, Y. Gao, Highly Self-Healable 3D Microsupercapacitor with MXene-Graphene Composite Aerogel, ACS Nano 12 (2018) 4224–4232.

[17] C. Körber, G. Rau, M.D. Cosman, E.G. Cravalho, Interaction of particles and a moving ice-liquid interface, J. Cryst. Growth 72 (1985) 649–662.

[18] B. Anasori, M.R. Lukatskaya, Y. Gogotsi, 2D metal carbides and nitrides (MXenes) for energy storage, Nat. Rev. Mater. 2 (2017).

[19] O. Mashtalir, M. Naguib, V.N. Mochalin, Y. Dall'Agnese, M. Heon, M.W. Barsoum, Y. Gogotsi, Intercalation and delamination of layered carbides and carbonitrides, Nat. Commun. 4 (2013) 1716.

[20] Y. Tong, M. He, Y. Zhou, X. Zhong, L. Fan, T. Huang, Q. Liao, Y. Wang, Hybridizing polypyrrole chains with laminated and two-dimensional Ti3C2Tx toward high-performance electromagnetic wave absorption, Appl. Surf. Sci. 434 (2018) 283–293.

[21] M. Naguib, V.N. Mochalin, M.W. Barsoum, Y. Gogotsi, 25th anniversary article: MXenes: a new family of two-dimensional materials, Adv. Mater. 26 (2014) 992–1005.

[22] H. Lv, Z. Yang, P.L. Wang, G. Ji, J. Song, L. Zheng, H. Zeng, Z.J. Xu, A Voltage-boosting strategy enabling a low-frequency, flexible electromagnetic wave absorption device, Adv. Mater. 30 (2018) e1706343.

[23] M. Li, M. Han, J. Zhou, Q. Deng, X. Zhou, J. Xue, S. Du, X. Yin, Q. Huang, Novel Scale-Like Structures of Graphite_TiC_Ti3C2 Hybrids for Electromagnetic Absorption, Adv. Electron. Mater. 4 (2018) 1700617.

[24] Y. Jiang, X. Xie, Y. Chen, Y. Liu, R. Yang, G. Sui, Hierarchically structured cellulose aerogels with interconnected MXene networks and their enhanced microwave absorption properties, J. Mater. Chem. C 6 (2018) 8679–8687.

[25] B. Dai, B. Zhao, X. Xie, T. Su, B. Fan, R. Zhang, R. Yang, Novel two-dimensional Ti3C2Tx MXenes_ nano-carbon sphere hybrids for high-performance microwave absorption, J. Mater. Chem. C 6 (2018) 5690–5697.

[26] X. Li, X. Yin, M. Han, C. Song, X. Sun, H. Xu, L. Cheng, L. Zhang, A controllable heterogeneous structure and electromagnetic wave absorption properties of Ti2CTx MXene, J. Mater. Chem. C 5 (2017) 7621–7628.

[27] S. Yan, C. Cao, J. He, L. He, Z. Qu, Investigation on the electromagnetic and broadband microwave absorption properties of Ti3C2 Mxene/flaky carbonyl iron composites, J. Mater. Sci.: Mater. Electron. 30 (2019) 6537–6543.

[28] J. Liu, H.B. Zhang, X. Xie, R. Yang, Z. Liu, Y. Liu, Z.Z. Yu, Multifunctional, Superelastic, and Lightweight MXene/Polyimide Aerogels, Small 14 (2018) e1802479.

[29] D.R. Clarke, Interpenetrating phase composites, J. Am. Ceram. Soc. 75 (1992) 20.

[30] B. Quan, X. Liang, G. Ji, J. Ma, P. Ouyang, H. Gong, G. Xu, Y. Du, Strong electromagnetic wave response derived from the construction of dielectric/magnetic media heterostructure and multiple interfaces, ACS Appl. Mater. Interfaces 9 (2017) 9964–9974.

[31] H. Sun, R. Che, X. You, Y. Jiang, Z. Yang, J. Deng, L. Qiu, H. Peng, Cross-stacking aligned carbon-nanotube films to tune microwave absorption frequencies and increase absorption intensities, Adv. Mater. 26 (2014) 8120–8125.

[32] H. Xu, X. Yin, M. Li, F. Ye, M. Han, Z. Hou, X. Li, L. Zhang, L. Cheng, Mesoporous carbon hollow microspheres with red blood cell like morphology for efficient microwave absorption at elevated temperature, Carbon 132 (2018) 343–351.

[33] M. Zhang, Z. Jiang, X. Lv, X. Zhang, Y. Zhang, J. Zhang, L. Zhang, C. Gong, Microwave absorption performance of reduced graphene oxide with negative imaginary permeability, J. Phys. D Appl. Phys. 53 (2020).

[34] E. Vazquez, M. Prato, Carbon nanotubes and microwaves: interactions, responses, and applications, ACS Nano 3 (2009) 3819–3824.

[35] M.-S. Cao, Y.-Z. Cai, P. He, J.-C. Shu, W.-Q. Cao, J. Yuan, 2D MXenes: Electromagnetic property for microwave absorption and electromagnetic interference shielding, Chem. Eng. J. 359 (2019) 1265–1302.

[36] B. Wen, M.-S. Cao, Z.-L. Hou, W.-L. Song, L. Zhang, M.-M. Lu, H.-B. Jin, X.-Y. Fang, W.-Z. Wang, J. Yuan, Temperature dependent microwave attenuation behavior for carbon-nanotube/silica composites, Carbon 65 (2013) 124–139.

[37] F. Wu, A. Xie, M. Sun, Y. Wang, M. Wang, Reduced graphene oxide (RGO) modified spongelike polypyrrole (PPy) aerogel for excellent electromagnetic absorption, J. Mater. Chem. A 3 (2015) 14358–14369.

[38] F. Shahzad, M. Alhabeb, C.B. Hatter, B. Anasori, S.M. Hong, C.M. Koo, Y. Gogotsi, Electromagnetic interference shielding with 2D transition metal carbides (MXenes), Science 353 (2016) 1137–1140.

[39] M. Cao, C. Han, X. Wang, M. Zhang, Y. Zhang, J. Shu, H. Yang, X. Fang, J. Yuan, Graphene nanohybrids: excellent electromagnetic properties for the absorbing and shielding of electromagnetic waves, J. Mater. Chem. C 6 (2018) 4586–4602.

[40] S. Liu, M. Zhang, X. Lv, Y. Wei, Y. Shi, J. Zhang, L. Zhang, C. Gong, Arousing

effective attenuation mechanism of reduced graphene oxide-based composites for lightweight and high efficiency microwave absorption, Appl. Phys. Lett. 113 (2018).

[41] B. Zhang, J. Wang, T. Wang, X. Su, S. Yang, W. Chen, J. Wang, J. Sun, J. Peng, High-performance microwave absorption epoxy composites filled with hollow nickel nanoparticles modified graphene via chemical etching method, Compos. Sci. Technol. 176 (2019) 54–63.

[42] H. Wang, F. Meng, C. Jing, J. Li, T. Li, Z. Chen, H. Luo, Z. Zhou, Carbonized design of hierarchical porous carbon/Fe$_3$O$_4$@Fe derived from loofah sponge to achieve tunable high-performance microwave absorption, ACS Sustainable Chem. Eng. 6 (2018) 11801–11810.

[43] Z. Ma, C.-T. Cao, Q.-F. Liu, J.-B. Wang, A new method to calculate the degree of electromagnetic impedance matching in one-layer microwave absorbers, Chin. Phys. Lett. 29 (2012).

[44] Y. Wei, L. Zhang, C. Gong, S. Liu, M. Zhang, Y. Shi, J. Zhang, Fabrication of TiN/Carbon nanofibers by electrospinning and their electromagnetic wave absorption properties, J. Alloy. Compd. 735 (2018) 1488–1493.